Moisture and moist static energy budgets of South Asian monsoon low pressure systems in GFDL AM4.0

Ángel F. Adames[1,2] and Yi Ming[1]

[1] *Geophysical Fluid Dynamics Laboratory/NOAA,*

Princeton, NJ

[2] *University Corporation for Atmospheric Research*

Boulder, CO

[*] *Corresponding author address: 201 Forrestal Rd*

Princetion, NJ, 08536

Email: Angel.Adames-Corraliza@noaa.gov

ABSTRACT

The mechanisms that lead to the propagation of anomalous precipitation in monsoon low and high pressure systems, collectively referred to as synoptic-scale monsoonal disturbances (SMDs), are investigated using daily output fields from GFDL's atmospheric general circulation model (AM4.0). On the basis of linear regression analysis of westard-propagating rainfall anomalies of timescales shorter than 15 days, it is found that SMDs are organized into wavetrains of 3-4 individual ciclones and anticyclones. These events amplify over the Bay of Bengal, reach a maximum amplitude over the eastern coast of India and dissipate as they approach the Arabian Sea.

It is also found that the precipitation anomalies in SMDs are highly correlated in space with column-integrated water vapor. Based on this correlation, we analyze the column moisture and frozen moist static energy (MSE) budgets as proxies for the propagation of the precipitation anomalies. Propagation of the moisture anomalies is dominated by vertical moisture advection while the MSE anomalies propagate due to horizontal advection of dry static energy by the anomalous winds. By combining the budgets, we interpret the propagation of the precipitation anomalies in terms of lifting that is forced by horizontal dry static energy advection, that is, ascent along sloping isentropes. This process moistens the lower free-troposphere, producing an environment that is conducive to deep convection. Longwave radiative heating is the main mechanism for maintaining MSE and precipitation anomalies.

1. Introduction

The Indian summer monsoon features large spatial and temporal variations in precipitation (Chang 2017). Among the transient disturbances that grow in these region are synoptic-scale cyclones that are often referred to as monsoon low pressure systems. These systems are characterized by slow westward and northward propagation and a horizontal radius of ∼2000 km (Godbole 1977; Krishnamurti and Chow 1975, 1976; Sikka 1977; Lau and Lau 1990). The India Meteorological Department (IMD) categorizes monsoon low pressure systems according to the strength of surface wind speed. The weakest systems are defined as lows, stronger systems with surface winds between 8.5 and 16.5 m s^{-1} are defined as monsoon depressions, and the strongest systems are referred to as cyclonic storms (Saha et al. 1981; Krishnamurthy and Ajayamohan 2010; Hunt et al. 2016). Anomalous anticyclones are also observed during the Indian monsoon, which have structures similar to the low pressure systems but with reversed polarity (Krishnamurthy and Ajayamohan 2010). We will collectively refer to the high and low pressure systems as synoptic-scale monsoonal disturbances (SMDs) (Krishnamurthy and Ajayamohan 2010; Ditchek et al. 2016).

During their lifecycle, monsoon low pressure systems often make landfall over the Indian subcontinent, producing up to half of the total monsoon rainfall received by India (Stano et al. 2002; Ding and Sikka 2006; Yoon and Chen 2005; Yoon and Huang 2012). Conversely, high pressure systems are associated with breaks in the monsoon, with little or no rainfall occurring during the passage of these systems. Thus, understanding SMDs is of critical importance to our understanding of the Indian monsoon and its variability.

In spite of the important role that SMDs have in the monsoon's hydrologic cycle, very few studies have analyzed how these systems modulate rainfall. Many studies have assumed that SMDs are a result of a variant of baroclinic instability called moist baroclinic instability (Salvekar et al. 1986; Krishnakumar et al. 1992; Krishnamurti et al. 2013, see also Cohen and Boos 2016 for a review on the topic), with precipitation being a result of large-scale quasi-geostrophic (QG) ascent in these disturbances (Shukla 1978; Mak 1983; Sanders

1984). Other studies have included moist convection in the form of frictional convergence feedbacks (Goswami 1987).

To our best knowledge, the first study to examine the water vapor budget of SMDs was Yoon and Chen (2005). They found that the leading balance in SMDs involves import of moisture through convergence and loss of moisture through condensation and precipitation. Their study, however, did not consider the Eulerian temporal tendency in moisture in the budget, neglecting it under the assumption that it contributed little to the total budget. However, recent studies have shown that SMDs are chatacterized by large moisture anomalies (Krishnamurthy and Ajayamohan 2010; Hunt et al. 2016). The large amplitude of specific humidity together with the $\sim$5 day timescale of SMDs suggests that the temporal tendency in moisture may not be negligible. Understanding the evolution of moisture, and the related moist static energy (MSE), may lead to novel insights into the dynamics of SMDs.

The goal of this study is to analyze the moisture and MSE budgets of SMDs. To carry out this analysis, we will make use of daily fields from GFDL's atmospheric general circulation model (AGCM). We use this model because it captures the main features of SMDs, and because it does not exhibit the large residuals in moisture/MSE budgets that reanalysis products have as a result of the data assimilation process (Mapes and Bacmeister 2012). Additionally, previous studies have shown that models are able to simulate SMDs reasonably well (Ashok et al. 2000; Sabre et al. 2000; Sø rland et al. 2016; Hunt and Turner 2017). We will show that the propagation of the moisture anomalies is dominated by vertical moisture advection while propagation of the MSE anomalies is dominated by horizontal MSE advection. While these two processes may seem distinct, we will show that horizontal dry static energy advection can induce vertical motion, which in turns induces a moisture tendency through vertical moisture advection.

This study is structured as follows. The next section describes AM4.0 and the methods of analysis. Section 3 describes the Indian monsoon mean state and variability as simulated by AM4. Section 4 and 5 discusses the moisture and moist static energy (MSE) budgets of SMDs, respectively. Section 6 synthesizes the results from the two budgets. A concluding discussion is offered in section 7.

2. Data and Methods

a. Model description

Most of the analysis presented here is made using daily output data from GFDL's AGCM (AM4.0, Zhao et al. 2017a,b). AM4.0 uses a finite volume, cubed-sphere topology with ∼100 km resolution per cube face. The output resolution used here is on a $1.25° \times 1°$ longitude-latitude grid. The model contains 33 vertical hybrid sigma-pressure levels (Simmons and Burridge 1981) extending from the surface to 1 hPa. Convection is parameterized in terms of a double plume scheme, which is similar to the shallow convection scheme described in Bretherton et al. (2004) but extended to include an additional plume to represent deep convection. Further details about the model configuration and its initial performance have been documented by Zhao et al. (2017a,b).

The simulations here are made using prescribed present-day sea surface temperature boundary conditions (Zhao et al. 2017a). The experiments are run for one year as spinup, and then run for an additional 10 years. We analyze the last 10 years of the simulation. Because we are mainly interested in the dynamics of SMDs in this model, we restrict our analysis to the boreal summer months of June through September (JJAS).

The following AM4.0 fields are used in this study: the horizontal winds (u,v), geopotential height (Z), specific humidity (q), precipitation (P), dry static energy (s), frozen moist static energy (h), surface and top of the atmosphere shortwave (SW) and longwave (LW) radiative fluxes, and surface sensible H and latent heat fluxes E. In addition to daily data from AM4.0, two other datasets are used in this study. We make use of the $1.5° \times 1.5°$ horizontal resolution, daily geopotential height and wind data from the ERA-Interim (Dee et al. 2011) for the 33-year time period of 1979-2011. Rainfall data from the Tropical Rainfall

Measurement Mission product 3B42 (TRMM-3B42, Huffman et al. 2007) is also used in this study.

b. Methods

Many of the results shown in the following sections are obtained through linear regression analysis, following the method described in Adames and Wallace (2014). We create a time series that describes the evolution of SMDs over the Bay of Bengal. Daily precipitation data, filtered to retain timescales shorter than 15 days and westward-propagating zonal wavenumbers 3-25 using the method of Hayashi (1979), is used to create this index. The filtered data was averaged over 85-90°E, 15-20°N, where monsoon low-pressure system activity is strongest (Sikka 1977; Godbole 1977; Boos et al. 2015). This method is similar to the method employed by Yoon and Chen (2005) and Chen et al. (2005). The statistical significance of the regression patterns was tested via a two-tailed t-test, and the contour and shading intervals are selected to roughly represent the 95% confidence interval.

In Section 3 we make use of space-time spectral analysis, following the methods of Wheeler and Kiladis (1999) and Hendon and Wheeler (2008). In order to extract the signal from SMDs, the time series of precipitation is divided into 60 day segments that overlap by 30 days. The segments are tapered to zero through the use of a Hanning window. We also use a Hanning window in longitude to emphasize tropical wave activity occurring over the longitude range of 50°-130°E. After tapering, complex fast Fourier transforms (FFTs) are computed in longitude and then in time. Finally, the power spectrum is averaged over all segments and over the 10°-25°N latitude belt. The number of degrees of freedom is calculated to be 121 [2 (amplitude and phase) $\times$ 10 (years) $\times$ 365 $\times$(days)/60 (segment length)]. We calculate the signal as $(P_{xx} - P_{red})/P_{xx}$, where P_{red} is the red spectrum, calculated using Eq. (1) of Masunaga (2007), and a value of 0.5 is considered to be statistically significant in this study. We have found the analysis to be insensitive to the length of the spatial Hanning window, or the choice of segment length as long as the SMD activity is captured by the spectral analysis.

In Sections 5 and 6 the moisture and frozen MSE budgets of SMDs are presented, respectively. Some of these budget terms exhibit large residuals due to numerical errors in the calculations of the budgets. These errors arise from the complex topography characteristic of South Asia, from the calculation of numerical gradients and from the interpolation from the model's native grid to the coordinate system used here. In order to reduce these residuals, we apply the adjustment method described in the Appendix of Hill et al. (2017). This method adds a barotropic adjustment to the horizontal wind field in order to satisfy conservation of column-integrated moisture/MSE. Using this method largely reduces the residual from these numerical errors.

Additionally, in Sections 5 and 6 we employ a compositing technique in space that smooths out small-scale noise in the South Asian monsoon, so that the synoptic-scale structure of the moisture and MSE budgets can be brought out more clearly. We will refer to this technique as an SMD composite. In this procedure, we generate multiple maps by shifting the longitude-latitude box of the SMD index (85-90°E, 15-20°N) by up to two degrees north/south and/or west/east. For example, regression maps are generated by using indices centered on 85-90°E, 14-19°N, or 85-90°E, 16-21°N. Each of these maps is then shifted such that the center of the moisture/MSE anomalies is centered over the 85-90°E, 15-20°N box. The SMD composite is then obtained by averaging all of the regression maps.

3. Monsoonal mean state and variability in AM4

Figure 1 shows the JJAS mean 850 hPa geopotential height and horizontal winds for AM4.0 and ERA-Interim. AM4.0 captures the main features of the monsoonal circulation. The simulated monsoon trough is is situated over northeast India, with the corresponding increase in height southward towards the Indian Ocean. A low-level westerly jet is seen in the area where the height gradient is strongest. There are also some differences with respect to ERA-Interim. AM4.0 exhibits stronger westerlies that extend further eastward past the Philippines, and the geopotential height gradient is stronger. The difference in the westerly jet is further shown in Fig. 2, along with moisture, precipitation and its variability. Mean precipitation (panels a and b) in AM4.0, while of similar magnitude to TRMM, occurs at different locations with respect to observations. While TRMM shows a rainfall maxima along the western coast of India and over the northeastern Bay of Bengal, AM4.0 instead exhibits a broader region of rainfall over northwest India that extends eastward and merges with a second region of maximum rainfall that is centered over the Bay of Bengal. The standard deviation of JJAS precipitation, shown in panel b, exhibits similar spatial patterns. Additionally, it is clear that TRMM precipitation exhibits a larger variance than the model does. This may be related to the inability of coarse-resolution GCMs to fully represent the topographic features of South Asia, thus not adequately representing their effects on precipitation.

Column-integrated water vapor, shown in Fig. 2c, exhibits horizontal pattern in AM4.0 that is consistent with reanalysis, although AM4.0 slightly overestimates column water in comparison to ERA-Interim. Column dry static energy, shown in panel (d), exhibits slightly smaller values in AM4.0 than in ERA-Interim. Nonetheless, the two datasets exhibit similar horizontal patterns, revealing that DSE increases with latitude during JJAS over southern Asia. It will be shown in subsequent sections that this positive meridional DSE gradient plays a central role in the propagation of the SMDs. Column MSE, shown in Fig. 2e is similar to column moisture, except the MSE maximum is shifted northward.

Figure 3a shows the JJAS signal strength of precipitation in AM4.0 averaged over the 10-25°N latitude belt. Variability in the South Asian monsoon region is dominated by westward-propagating synoptic-scale disturbances (zonal wavenumbers 3-25) with timescales between 3-15 days. This range of zonal and temporal scales is consistent with the documented scale of SMDs (Sikka 1977; Godbole 1977; Stano et al. 2002; Hunt et al. 2016). A weaker signal is also seen at eastward-propagating zonal wavenumbers 1-20 and timescales longer than 30 days, likely in association with the boreal summer intraseasonal oscillation (BSISO). In comparison, the signal strength for TRMM-3B42 rainfall, shown in Fig. 3b, is slightly weaker, but shows a nearly identical signal, with peak strength also occurring near zonal wavenumber 10 and 5-day timescales.

Based on the space-time variability in Fig. 3, we construct a SMD index by filtering daily precipitation in order to retain westward-propagating zonal wavenumbers 3-25 and timescales of 15 days and shorter (dashed box in Fig. 3). We have verified that our results are robust to different choices of the filter as long as the frequencies and wavenumbers where SMD activity is strongest is included (see Fig. 3). The filtered precipitation field is then averaged over the 85-90°E, 15-20°N box. Regression maps of the horizontal structure of SMDs is shown in Fig. 4. At lag day -2 an anticyclonic feature is seen over northeast India, with negative precipitation anomalies centered near and to the west of the maximum height anomalies. This anticyclone reaches a peak amplitude over India and dissipates as it reaches the Arabian sea at lag day 1. The anomalous anticyclone is followed by a cyclonic anomaly coupled to enhanced precipitation. The region of enhanced rainfall is first seen developing near the coast of Myanmar at lag day -2. At lag day -1 the precipitation anomalies have amplified and propagated west towards the Bay of Bengal. These anomalies are centered between the minimum height anomalies and anomalous northerly flow, consistent with observations (Warner 1984; Chen et al. 2005; Hunt et al. 2016), and other modeling studies (Ashok et al. 2000; Sabre et al. 2000; Hunt and Turner 2017). In subsequent days the region of enhanced precipitation follows a pattern similar to the anticyclone that preceded it. The horizontal structure and propagation of the depressions in Fig. 4 are similar to those seen in Fig. 2 of Daggupaty and Sikka (1977) and Fig. 4 of Yoon and Chen (2005).

We can obtain some insights onto the vertical structure of the simulatd SMDs by analyzing longitude-height cross sections. Figure 5 shows a cross section of anomalous geopotential height Z', meridional winds v', vertical velocity ω' and specific humidity q overlaid by the meridionally-averaged zonal mass circulation $(\rho u', \rho w')$. Z' and v' are largely confined to the lower troposphere, with both exhibiting maximum amplitudes near the surface with little signature in the upper troposphere. ω' is a maximum in the mid-troposphere, exhibiting a structure reminiscent of a first baroclinic mode in vertical motion. q; is largely confined to the lowest levels of the troposphere, exhibiting a maximum between 850-900 hPa near 88°E and a minimum ∼75°E and 650 hPa. Both q' and, to a lesser degree, v' exhibit westward tilt with height, possibly as a result of the low-level monsoon jet advecting the anomalies more strongly near the surface.

An interesting feature about the cross sections in Figs. 5a-b is the phasing between the fields. Both ω' and q' are shifted west of the region of low pressure, with ω' exhibiting a larger shift than q'. To further elucidate this phasing, Fig. 5c shows precipitation, column water vapor and vertical velocity averaged over the same latitudinal belt. Column water vapor and precipitation exhibit an in-phase relationship while mid-tropospheric ascent leads both fields by ∼5° of longitude. All three fields are, in turn, shifted westward with respect to the center of the height anomalies.

Figure 6 shows a time-longitude diagram of anomalous precipitation associated with SMDs. It is clear from this diagram that the SMDs are arranged into a packet of 3-4 westward-propagating vortices. Each event propagates westward with a phase speed of ~ -4 m s^{-1}. The maximum amplitude of each event progressively shifts eastward, indicating that the wavetrain might be characterized by an eastward group velocity.

4. Column-integrated moisture budget

In the previous section we analyzed the mean state and variability in the South Asian monsoon as simulated by AM4. Precipitation variability in this region is found to be dominated by synoptic-scale features that resemble SMDs. In this section, we will seek to understand the evolution of the precipitation anomalies in these systems by analyzing the evolution of column-integrated moisture. Figure 7a shows column integrated moisture and precipitation in a SMD composite. The two fields are spatially correlated, with enhanced precipitation located in regions of enhanced moisture and vice versa for regions of suppressed precipitation. The correlation is more clear in Fig. 8, which shows the two fields in a scatterplot. A robust correlation of 0.84 is observed further suggesting a strong coupling between the two fields. We can thus define the precipitation anomalies as proportional to $\langle q' \rangle$ divided by a convective moisture adjustment timescale: $P' = \langle q' \rangle / \tau_c$. Through linear least-squares fit we find that the two fields are related by a timescale of ~ 4.5 hours.

Based on the strong correlation between column moisture and precipitation in these depression systems, we invoke the anomalous column-integrated moisture budget to understand the temporal evolution of precipitation in these systems

$$\frac{\partial \langle q' \rangle}{\partial t} = -\langle \mathbf{V} \cdot \nabla q \rangle' - \left\langle \omega \frac{\partial q}{\partial p} \right\rangle' + E' - P' \tag{1}$$

where $\mathbf{V}$ is the horizontal wind field, ω is the pressure velocity, and E' is the anomalous surface evaporation. Angle brackets correspond to vertical integration from 1000 hPa to 100 hPa, and primed angle brackets correspond to the same integral but for 15 day highpass filtered fields.

The contribution of each term in Eq. (1) to the propagation of the moisture anomalies is shown in Figs. 7 and 9. Precipitation (Fig. 7a) and vertical moisture advection (Fig. 7b) are the dominant terms and largely cancel one another. The sum of the two terms (Fig. 9b), which we will refer as the column moist process, is $\sim$15% as large as the individual terms that compose it. It moistens the atmosphere in regions anomalous northerly flow, and dries in regions of southerly flow. Column moist processes are largely in-phase with the moisture tendency in Fig. 9a, although they do not exhibit the poleward tilt with longitude that the column moisture tendency shows (panel a). This result indicates that ascent, which was shown to be shifted westward of $\langle q' \rangle$ in Fig. 5, moistens the atmosphere prior to the maximum in anomalous precipitation. The sum of all the budget terms yields a negligibly small residual (not shown).

In comparison, horizontal moisture advection is largely in-phase with the moisture anomalies and acts to damp them, with an additional component that shifts the moisture tendency poleward. Surface evaporation anomalies, shown in Fig 9c contributes little to the propagation of the moisture anomalies, only exhibiting anomalies over the Bay of Bengal.

We can assess the relative importance of the terms in Eq. (1) to the maintenance and propagation of $\langle q' \rangle$ by comparing their projections upon the $\langle q' \rangle$ and its tendency, following the methods of Andersen and Kuang (2012); Arnold et al. (2013) and Adames et al. (2016)

$$S_m(F) = \frac{||F \cdot \langle q' \rangle||}{||\langle q' \rangle \cdot \langle q' \rangle||} \tag{2a}$$

$$S_p(F) = \frac{||F \cdot \partial \langle q' \rangle / \partial t||}{||\partial \langle q' \rangle / \partial t \cdot \partial \langle q' \rangle / \partial t||} \tag{2b}$$

where F corresponds to the right-hand-side terms in Eq. (1). The contribution of each term to the propagation and maintenance of the moisture anomalies is shown in Fig. 10. It is clear that the propagation of the moisture anomalies is dominated by column moist processes, with little contribution from horizontal moisture advection and surface evaporation. Column processes imports moisture into the low-pressure system, maintaining the region of anomalous precipitation against dissipation from horizontal moisture advection.

5. Frozen moist static energy budget

In the previous section we analyzed the column-integrated moisture budget in order to understand the propagation of the precipitation anomalies in SMDs. It was shown that the difference between vertical moisture advection and precipitation dominates the propagation and maintenance of the moisture anomalies. In this section, we will analyze the column-integrated frozen MSE (denoted by h) budget. We define the frozen moist static energy as:

$$h = C_p T + gZ + L_v q - L_f q_i \tag{3}$$

where T is temperature, q_i is the ice mixing ratio, L_v is the latent energy of vaporization, L_f is the latent energy of fusion and C_p is the specific heat of dry air at constant pressure.

The MSE budget takes the following form

$$\frac{\partial \langle h' \rangle}{\partial t} \simeq -\langle \mathbf{V} \cdot \nabla h \rangle' - \left\langle \omega \frac{\partial h}{\partial p} \right\rangle' + \langle LW' \rangle + \langle SW' \rangle + H' + L_v E' \qquad (4)$$

where LW' and SW' are the longwave and shortwave radiative heating anomalies, respectively and H' is the surface sensible heat flux. Note that the left-hand-side can be more accurately described by the sum of internal energy and potential energy (Hill et al. 2017), and h is commonly used as an approximation.

The column frozen MSE anomalies along with their tendency are shown in Fig. 9f. The $\langle h \rangle$ anomalies are broadly similar to the $\langle q \rangle$ anomalies shown in the left column, indicating that $\langle h \rangle$ is dominated by the contribution from moisture. $\partial \langle h' \rangle / \partial t$ also exhibits a similar horizontal pattern to $\partial \langle q' \rangle / \partial t$.

The leading terms in the $\langle h' \rangle$ budget are shown in the right column of Fig. 9. The largest contribution to the propagation of $\langle h' \rangle$ is horizontal MSE advection. This pattern differs significantly than that of horizontal moisture advection in Fig. 9b, indicating that is dominated by the advection of dry static energy (DSE). Instead, horizontal MSE advection nearly matches the pattern of $\partial \langle h' \rangle / \partial t$ and is similar to the spatial pattern of the column moisture process. Vertical MSE advection acts to offset horizontal MSE advection but it is also shifted slightly eastward, acting to damp the MSE anomalies. Anomalous longwave radiative heating, while exhibiting smaller amplitude, is largely in phase with the MSE anomalies.

The results shown in Fig. 9 indicate that horizontal DSE advection is key to the propagation of the MSE anomalies. To further elucidate the physical processes that dominate horizontal MSE advection, we separate it into contribution arising from interactions from different temporal scales, following the methods of Maloney (2009); Kiranmayi and Maloney (2011) and Adames et al. (2016):

$$-\langle \mathbf{V} \cdot \nabla h \rangle' \simeq -\langle \mathbf{V}' \cdot \nabla \overline{h} \rangle' - \langle \overline{\mathbf{V}} \cdot \nabla h' \rangle' - \langle \mathbf{V}' \cdot \nabla h' \rangle' \qquad (5)$$

where overbars denote 15-day lowpass filtered data. The terms on the right-hand side of

Eq. (5) correspond to horizontal advection of low-frequency MSE by the high-frequency winds, horizontal advection of high-frequency MSE by the low-frequency winds, and the nonlinear advection of anomalous MSE by the anomalous winds. The contribution of each term to horiozntal MSE advection is shown in Fig. 11. It is clear that horizontal advection of low-frequency MSE by the high-frequency winds dominates, and explains the majority of the MSE tendency. The other two terms are small, and only contribute to shift the MSE tendency northward. The sum of the three terms approximately captures the total horizontal MSE advection shown in Fig. 9g. Since horizontal MSE advection is dominated by the DSE component, this result implies that advection of the mean DSE in Fig. 2d by the anomalous winds is the largest contributor to horizontal MSE advection.

The contribution of each term to the propagation and maintenance of MSE is shown in Fig. 10b. It is clear that horizontal MSE advection is the largest contributor to the propagation of the MSE anomalies, with some offset from vertical MSE advection. Longwave radiative heating maintains MSE against vertical MSE advection.

6. Bridging the budgets

In Sections 4 and 5 we analyzed the column moisture and moist static energy budgets, respectively, to understand the propagation of anomalous precipitation in SMDs. We found that the difference between vertical moisture advection and precipitation dominates the propagation of the moisture anomalies, while horizontal DSE advection dominates the propagation of the MSE anomalies. In this section we will show how these two processes are physically related. The column temperature trend in the simulated SMDs are $\sim$8% as large as the column apparent heating (not shown). If we neglect the temperature tendency in the thermodynamic energy equation, the leading balance occurs between horizontal temperature advection, vertical DSE advection and apparent heating. We may write this balance in terms of the dry static energy budget with little loss of accuracy, as described by Sobel et al. (2014)

$$\left(\omega\frac{\partial s}{\partial p}\right)' \simeq -(\mathbf{V}\cdot\nabla s)' + Q_c' + Q_r' \tag{6}$$

where Q_c' and Q_r' are the convective and radiative contributions to apparent heating. Following the method of Chikira (2014) and Adames (2017), we can separate the pressure velocity term into three contributions, one from horizontal DSE advection, one from radiative heating and one from convective heating $\omega \simeq \omega_a + \omega_r + \omega_c$. If we assume that perturbations in the vertical DSE gradient are much smaller than those of the background DSE gradient, we can obtain the following

$$\omega_a' \simeq -(\partial\overline{s}/\partial p)^{-1}(\mathbf{V}\cdot\nabla s)' \tag{7a}$$

$$\omega_c' \simeq (\partial\overline{s}/\partial p)^{-1}Q_c' \tag{7b}$$

$$\omega_r' \simeq (\partial\overline{s}/\partial p)^{-1}Q_r' \tag{7c}$$

where the overbar refers to timescales longer than 15 days. Note that ω_a' is adiabatically-driven while $\omega_c' + \omega_r'$ is diabatically-driven.

By combining Eq. (1) and (7) it becomes clear that vertical moisture advection is composed by a component that is driven by apparent heating, and an additional contribution that is forced by horizontal DSE advection. The former implies vertical motion in regions of apparent heating while the latter implies ascent in regions of positive DSE advection (i.e. warm air advection). Thus, ω_a' is related to ascent that occurs as air parcels move along sloping isentropic surfaces (isentropic ascent). The contribution of isentropic ascent and diabatic heating to total vertical motion is shown in Fig. 12*a*. Ascent driven by diabatic heating is the dominant term and predominantly contributes to the maintenance of the moisture anomalies. Ascent driven by positive DSE advection is smaller in magnitude and is responsible for shifting the vertical velocity anomalies west of the region of maximum precipitation. A small residual exists, likely due to errors in the analysis and vertical motion driven by nonlinear terms. It is clear from Fig. 12b that ω_a' is largely in phase with

$\partial\langle q'\rangle\partial t$, with a spatial correlation of ~0.9 (not shown). Thus ω_a' predominantly contributes to propagation of the SMDs by advecting moisture vertically in regions of isentropic ascent:

$$\frac{\partial\langle q'\rangle}{\partial t} \sim -\left\langle \omega_a' \frac{\partial \overline{q}}{\partial p} \right\rangle \tag{8}$$

Thus, that horizontal MSE advection dominates the propagation of the MSE anomalies is consistent with column processes dominating the propagation of the moisture anomalies. Equation (8) is a departure from the typical assumptions made for SMDs, where the quasi-geostrophic (QG) omega equation (See Eq. 6.34 in Holton 2004) is used to diagnose precipitation ($P' \propto \omega_a'$) and moisture tendencies are ignored (Rao and Rajamani 1970; Sanders 1984; Chen et al. 2005).

Similarly, anomalous radiative heating induces vertical motion that acts to maintain the anomalous precipitation in SMDs. Thus, that radiative heating maintains the MSE anomalies is consistent with column processes dominating the maintenance of the moisture anomalies.

7. Concluding Discussion

In this study we analyzed the column moisture and MSE budgets of synoptic-scale monsoon disturbances (SMDs) as simulated by GFDL's AM4.0. AM4.0 captures a mean JJAS flow and horizontal distributions of moisture, DSE and MSE that are consistent with those of ERA-Interim. However, the model fails to accurately describe the distribution of climatological-mean precipitation. In spite of this caveat, the model captures SMDs that are consistent with observations (Daggupaty and Sikka 1977; Chen et al. 2005). This result suggests that SMDs might not be sensitive to the details of the climatological-mean distribution of precipitation.

The simulated SMDs are found to exhibit a life cycle where they develop over the Bay of Bengal, attain a maximum amplitude as they make landfall over India and then dissipate as they reach the Arabian Sea. A lag regression analysis reveals that these systems are arranged into wavetrains of 3-4 events that propagate westward.

The processes that maintain and propagate these SMDs are analyzed on the basis of column-integrated moisture and MSE budgets. In the moisture budget, it is found that the sum of vertical moisture advection and precipitation (column processes) dominates both the propagation and maintenance of the low-pressure system. This moisture tendency results from anomalous vertical moisture advection slightly leading the precipitation anomalies as the SMD propagates westward, indicating that vertical moisture advection from deep ascent moistens the atmosphere prior to the maximum in anomalous precipitation. Similarly, vertical moisture advection maintains the precipitation anomalies against damping by horizontal advection.

The column MSE budget reveals that the processes that maintain the SMDs differ from those that induce its propagation. Horizontal MSE advection dominates the propagation of the MSE anomalies. Because the horizontal structure of MSE advection differs from that of horizontal moisture advection, it can be inferred that it is dominated by the DSE component. When both MSE and moisture budgets are considered together, and by assuming that the column-integrated temperature tendency in these disturbances is negligible, it is found that horizontal DSE advection induces vertical motion. This ascent, in turn, moistens the atmosphere to the west of the maximum precipitation anomalies. Ascent driven by horizontal DSE advection corresponds to lifting ocurring along isentropic surfaces.

In contrast, it is found that longwave radiative heating maintains the MSE anomalies against dissipation from horizontal moisture advection. This anomalous heating induces vertical motion which supplies the precipitation anomalies with additional water vapor. The same mechanism is suggested to play a key role in the maintenance of the MJO (Andersen and Kuang 2012; Chikira 2014; Sobel et al. 2014; Wolding et al. 2016) and in convective self-aggregation (Bretherton et al. 2005; Wing and Emanuel 2014).

Many studies have used the quasi-geostrophic (QG) approximation to analyze the propagation of monsoon depressions, using the QG omega equation to diagnose the region of anomalous precipitation (Mak 1982; Sanders 1984). However, we found that vertical motion is not directly related to precipitaiton. Instead, it is column moisture that is spatially correlated to precipitation, and vertical motion is found to be more closely related to the moisture tendency. This is a large departure from QG theory. This departure is important as it indicates that QG cannot account for the evolution of convection in these systems. Instead, vertical motion, water vapor and precipitation interact with each other, with isentropic lift acting increase column water vapor, which in turn produces a thermodynamic environment that favors increased precipitation.

There are a few limitations to this study. While moisture is the largest contributor to MSE, it only accounts for ~75% of the total vertically-integrated MSE (not shown). Thus, DSE accounts for roughly a quarter of the total frozen MSE, a non-negligible amount. Thus, the approximations shown in Section 6, while informative, are only qualitative. A rigorous, vertically-resolved analysis of moisture, ice and other thermodynamic variables could further elucidate the mechanisms that drive SMDs. Nonetheless, the results presented in this study indicate that analyzing moisture and MSE budgets provide useful insights on the structure and propagation of SMDs. Furthermore, incorporating these equations into a linear theoretical framework for monsoon depressions may also shed light on our understanding of these systems. Such a framework is presented in a companion paper.

Acknowledgments. This work was supported by the National Oceanic and Atmospheric Administration (NOAA) grant NA15OAR4310099. We would like to thank Isaac Held and Kuniaki Inoue for comments that have helped improve the manuscript. We would also like to thank Ming Zhao for making the AM4.0 data available to us.

REFERENCES

Adames, A. F., 2017: Precipitation Budget of the Madden-Julian Oscillation. *J. Atmos. Sci.*, **74 (6)**, 1799–1817, doi:10.1175/JAS-D-16-0242.1, URL https://doi.org/10.1175/JAS-D-16-0242.1, https://doi.org/10.1175/JAS-D-16-0242.1.

Adames, Á. F., and J. M. Wallace, 2014: Three-Dimensional Structure and Evolution of the MJO and Its Relation to the Mean Flow. *J. Atmos. Sci.*, **71 (6)**, 2007–2026.

Adames, . F., J. M. Wallace, and J. M. Monteiro, 2016: Seasonality of the structure and propagation characteristics of the MJO. *J. Atmos. Sci.*, **0 (0)**, null, doi:10.1175/JAS-D-15-0232.1, URL http://dx.doi.org/10.1175/JAS-D-15-0232.1, http://dx.doi.org/10.1175/JAS-D-15-0232.1=.

Andersen, J. A., and Z. Kuang, 2012: Moist Static Energy Budget of MJO-like Disturbances in the Atmosphere of a Zonally Symmetric Aquaplanet. *J. Climate*, **25 (8)**, 2782–2804.

Arnold, N. P., Z. Kuang, and E. Tziperman, 2013: Enhanced MJO-like Variability at High SST. *J. Climate*, **26 (3)**, 988–1001.

Ashok, K., M. K. Soman, and V. Satyan, 2000: Simulation of monsoon disturbances in a gcm. *pure and applied geophysics*, **157 (9)**, 1509–1539, doi:10.1007/PL00001131, URL https://doi.org/10.1007/PL00001131.

Boos, W. R., J. V. Hurley, and V. S. Murthy, 2015: Adiabatic westward drift of indian monsoon depressions. *Quarterly Journal of the Royal Meteorological Society*, **141 (689)**, 1035–1048, doi:10.1002/qj.2454, URL http://dx.doi.org/10.1002/qj.2454.

Bretherton, C. S., P. N. Blossey, and M. Khairoutdinov, 2005: An energy-balance analysis of deep convective self-aggregation above uniform SST. *J. Atmos. Sci.*, **62 (12)**, 4273–4292.

Bretherton, C. S., J. R. McCaa, and H. Grenier, 2004: A new parameterization for shallow cumulus convection and its application to marine subtropical cloud-topped boundary layers. part i: Description and 1d results. *Monthly Weather Review*, **132 (4)**, 864–882, doi:10.1175/1520-0493(2004)132⟨0864:ANPFSC⟩2.0.CO;2, URL https://doi.org/10.1175/1520-0493(2004)132⟨0864:ANPFSC⟩2.0.CO;2.

Chang, C.-P., 2017: *The global monsoon system: research and forecast*, Vol. 5. World Scientific.

Chen, T.-C., J.-H. Yoon, and S.-Y. Wang, 2005: Westward propagation of the indian monsoon depression. *Tellus A*, **57 (5)**, 758–769, doi:10.1111/j.1600-0870.2005.00140.x, URL http://dx.doi.org/10.1111/j.1600-0870.2005.00140.x.

Chikira, M., 2014: Eastward-propagating intraseasonal oscillation represented by Chikira–Sugiyama cumulus parameterization. Part II: Understanding moisture variation under weak temperature gradient balance. *J. Atmos. Sci.*, **71 (2)**, 615–639.

Cohen, N. Y., and W. R. Boos, 2016: Perspectives on moist baroclinic instability: Implications for the growth of monsoon depressions. *Journal of the Atmospheric Sciences*, **73 (4)**, 1767–1788, doi:10.1175/JAS-D-15-0254.1, URL http://dx.doi.org/10.1175/JAS-D-15-0254.1, http://dx.doi.org/10.1175/JAS-D-15-0254.1.

Daggupaty, S. M., and D. R. Sikka, 1977: On the vorticity Budget and Vertical Velocity Distribution Associated with the Life Cycle of a Monsoon Depression. *Journal of the Atmospheric Sciences*, **34 (5)**, 773–792, doi:10.1175/1520-0469(1977)034⟨0773:OTVBAV⟩2.0.CO;2, URL https://doi.org/10.1175/1520-0469(1977)034⟨0773:OTVBAV⟩2.0.CO;2, https://doi.org/10.1175/1520-0469(1977)034⟨0773:OTVBAV⟩2.0.CO;2.

Dee, D. P., and Coauthors, 2011: The ERA-Interim reanalysis: configuration and performance of the data assimilation system. *Quart. J. Roy. Meteor. Soc.*, **137 (656)**, 553–597.

Ding, Y., and D. R. Sikka, 2006: *Synoptic systems and weather*, 131–201. Springer Berlin Heidelberg, Berlin, Heidelberg, doi:10.1007/3-540-37722-0_4, URL http://dx.doi.org/10.1007/3-540-37722-0_4.

Ditchek, S. D., W. R. Boos, S. J. Camargo, and M. K. Tippett, 2016: A Genesis Index for Monsoon Disturbances. *Journal of Climate*, **29 (14)**, 5189–5203, doi:10.1175/JCLI-D-15-0704.1, URL https://doi.org/10.1175/JCLI-D-15-0704.1, https://doi.org/10.1175/JCLI-D-15-0704.1.

Godbole, R. V., 1977: The composite structure of the monsoon depression. *Tellus*, **29 (1)**, 25–40, doi:10.1111/j.2153-3490.1977.tb00706.x, URL http://dx.doi.org/10.1111/j.2153-3490.1977.tb00706.x.

Goswami, B. N., 1987: A mechanism for the west-north-west movement of monsoon depressions. *Nature*, **326 (6111)**, 376–378, URL http://dx.doi.org/10.1038/326376a0.

Hayashi, Y., 1979: A Generalized Method of Resolving Transient Disturbances into Standing and Traveling Waves by Space-Time Spectral Analysis. *J. Atmos. Sci.*, **36 (6)**, 1017–1029.

Hendon, H. H., and M. C. Wheeler, 2008: Some Space-Time Spectral Analyses of Tropical Convection and Planetary-Scale Waves. *J. Atmos. Sci.*, **65 (9)**, 2936–2948.

Hill, S. A., Y. Ming, I. M. Held, and M. Zhao, 2017: A moist static energy budget-based analysis of the sahel rainfall response to uniform oceanic warming. *Journal of Climate*, **0 (0)**, In Press, doi:10.1175/JCLI-D-16-0785.1, URL https://doi.org/10.1175/JCLI-D-16-0785.1, https://doi.org/10.1175/JCLI-D-16-0785.1.

Holton, J. R., 2004: *An Introduction to Dynamic Meteorology*, Vol. 4. Elsevier Academic, 535 pp.

Huffman, G. J., and Coauthors, 2007: The TRMM Multisatellite Precipitation Analysis (TMPA): Quasi-Global, Multiyear, Combined-Sensor Precipitation Estimates at Fine Scales. *Journal of Hydrometeorology*, **8 (1)**, 38–55.

Hunt, K. M., and A. G. Turner, 2017: The effect of horizontal resolution on indian monsoon depressions in the met office nwp model. *Quarterly Journal of the Royal Meteorological*

Society, **143 (705)**, 1756–1771, doi:10.1002/qj.3030, URL http://dx.doi.org/10.1002/qj.3030.

Hunt, K. M. R., A. G. Turner, P. M. Inness, D. E. Parker, and R. C. Levine, 2016: On the structure and dynamics of indian monsoon depressions. *Monthly Weather Review*, **144 (9)**, 3391–3416, doi:10.1175/MWR-D-15-0138.1, URL http://dx.doi.org/10.1175/MWR-D-15-0138.1, http://dx.doi.org/10.1175/MWR-D-15-0138.1.

Kiranmayi, L., and E. D. Maloney, 2011: Intraseasonal moist static energy budget in reanalysis data. *J. Geophys. Res.*, **116 (D21)**, 1–12.

Krishnakumar, V., R. N. Keshavamurty, and S. V. Kasture, 1992: Moist baroclinic instability and the growth of monsoon depressions— linear and nonlinear studies. *Proceedings of the Indian Academy of Sciences - Earth and Planetary Sciences*, **101 (2)**, 123–152, doi:10.1007/BF02840349, URL http://dx.doi.org/10.1007/BF02840349.

Krishnamurthy, V., and R. S. Ajayamohan, 2010: Composite structure of monsoon low pressure systems and its relation to indian rainfall. *Journal of Climate*, **23 (16)**, 4285–4305, doi:10.1175/2010JCLI2953.1, URL http://dx.doi.org/10.1175/2010JCLI2953.1, http://dx.doi.org/10.1175/2010JCLI2953.1.

Krishnamurti, K. M. G. R. C. C.-B. C. F., T.-N., and J. H. Chow, 1975: Study of a monsoon depression (I): synoptic structure. *J. Meteorol. Soc. Japan*, **53**, 227–239, doi:10.1175/JAS3741.1.

Krishnamurti, K. M. G. R. C. C.-B. C. F., T.-N., and J. H. Chow, 1976: Study of a monsoon depression (II): dynamical structure. *J. Meteorol. Soc. Japan*, **54**, 208–226, doi:10.1175/JAS3741.1.

Krishnamurti, T. N., A. Martin, R. Krishnamurti, A. Simon, A. Thomas, and V. Kumar, 2013: Impacts of enhanced ccn on the organization of convection and recent reduced counts of monsoon depressions. *Climate Dynamics*, **41 (1)**, 117–134, doi: 10.1007/s00382-012-1638-z, URL http://dx.doi.org/10.1007/s00382-012-1638-z.

Lau, K.-H., and N.-C. Lau, 1990: Observed structure and propagation characteristics of tropical summertime synoptic scale disturbances. *Monthly Weather Review*, **118 (9)**, 1888–1913, doi:10.1175/1520-0493(1990)118⟨1888:OSAPCO⟩2.0.CO;2, URL https://doi.org/10.1175/1520-0493(1990)118⟨1888:OSAPCO⟩2.0.CO;2, https://doi.org/10.1175/1520-0493(1990)118⟨1888:OSAPCO⟩2.0.CO;2.

Mak, M., 1982: On Moist Quasi-Geostrophic Baroclinic Instability. *Journal of the Atmospheric Sciences*, **39 (9)**, 2028–2037, doi:10.1175/1520-0469(1982)039⟨2028:OMQGBI⟩2.0.CO;2, URL https://doi.org/10.1175/1520-0469(1982)039⟨2028:OMQGBI⟩2.0.CO;2, https://doi.org/10.1175/1520-0469(1982)039⟨2028:OMQGBI⟩2.0.CO;2.

Mak, M., 1983: A moist baroclinic model for monsoonal mid-tropospheric cyclogenesis. *Journal of the Atmospheric Sciences*, **40 (5)**, 1154–1162, doi:10.1175/1520-0469(1983)040⟨1154:AMBMFM⟩2.0.CO;2, URL https://doi.org/10.1175/1520-0469(1983)040⟨1154:AMBMFM⟩2.0.CO;2, https://doi.org/10.1175/1520-0469(1983)040⟨1154:AMBMFM⟩2.0.CO;2.

Maloney, E. D., 2009: The moist static energy budget of a composite tropical intraseasonal oscillation in a climate model. *J. Climate*, **22 (3)**, 711–729.

Mapes, B. E., and J. T. Bacmeister, 2012: Diagnosis of Tropical Biases and the MJO from Patterns in the MERRA Analysis Tendency Fields. *J. Climate*, **25 (18)**, 6202–6214.

Masunaga, H., 2007: Seasonality and regionality of the Madden- Julian oscillation, Kelvin wave and equatorial Rossby wave. *J. Atmos. Sci.*, **64**, 4400–4416, doi:10.1175/2007JAS2179.1.

Rao, K., and S. Rajamani, 1970: Diagnostic study of a monsoon depression by geostrophic baroclinic model. *Indian Journal of Meteorology and Geophysics*, **21**, 187–194.

Sabre, M., K. Hodges, K. Laval, J. Polcher, and F. Désalmand, 2000: Simulation of monsoon disturbances in the lmd gcm. *Monthly Weather Review*, **128 (11)**, 3752–3771, doi:10.1175/1520-0493(2001)129⟨3752:SOMDIT⟩2.0.CO;2, URL https://doi.org/10.1175/1520-0493(2001)129⟨3752:SOMDIT⟩2.0.CO;2, https://doi.org/10.1175/1520-0493(2001)129⟨3752:SOMDIT⟩2.0.CO;2.

Saha, K., F. Sanders, and J. Shukla, 1981: Westward Propagating Predecessors of Monsoon Depressions. *Monthly Weather Review*, **109 (2)**, 330–343, doi:10.1175/1520-0493(1981)109⟨0330:WPPOMD⟩2.0.CO;2, URL https://doi.org/10.1175/1520-0493(1981)109⟨0330:WPPOMD⟩2.0.CO;2, https://doi.org/10.1175/1520-0493(1981)109⟨0330:WPPOMD⟩2.0.CO;2.

Salvekar, P. S., L. George, and S. K. Mishra, 1986: Low level wind shear and baroclinic growth of monsoon depression scale waves. *Meteorology and Atmospheric Physics*, **35 (1)**, 10–18, doi:10.1007/BF01029520, URL http://dx.doi.org/10.1007/BF01029520.

Sanders, F., 1984: Quasi-geostrophic diagnosis of the monsoon depression of 5-8 july 1979. *Journal of the Atmospheric Sciences*, **41 (4)**, 538–552, doi:10.1175/1520-0469(1984)041⟨0538:QGDOTM⟩2.0.CO;2, URL https://doi.org/10.1175/1520-0469(1984)041⟨0538:QGDOTM⟩2.0.CO;2, https://doi.org/10.1175/1520-0469(1984)041⟨0538:QGDOTM⟩2.0.CO;2.

Shukla, J., 1978: Cisk-barotropic-baroclinic instability and the growth of monsoon depressions. *Journal of the Atmospheric Sciences*, **35 (3)**, 495–508, doi:10.1175/1520-0469(1978)035⟨0495:CBBIAT⟩2.0.CO;2, URL http://dx.doi.org/10.1175/1520-0469(1978)035⟨0495:CBBIAT⟩2.0.CO;2, http://dx.doi.org/10.1175/1520-0469(1978)035⟨0495:CBBIAT⟩2.0.CO;2.

Sikka, D. R., 1977: Some aspects of the life history, structure and movement of monsoon depressions. *pure and applied geophysics*, **115 (5)**, 1501–1529, doi:10.1007/BF00874421, URL http://dx.doi.org/10.1007/BF00874421.

Simmons, A. J., and D. M. Burridge, 1981: An energy and angular-momentum conserving vertical finite-difference scheme and hybrid vertical coordinates. *Monthly Weather Review*, **109 (4)**, 758–766, doi:10.1175/1520-0493(1981)109⟨0758:AEAAMC⟩2.0.CO;2, URL https://doi.org/10.1175/1520-0493(1981)109⟨0758:AEAAMC⟩2.0.CO;2, https://doi.org/10.1175/1520-0493(1981)109⟨0758:AEAAMC⟩2.0.CO;2.

Sø rland, S. L., A. Sorteberg, C. Liu, and R. Rasmussen, 2016: Precipitation response of monsoon low-pressure systems to an idealized uniform temperature increase. *Journal of Geophysical Research: Atmospheres*, **121 (11)**, 6258–6272, doi:10.1002/2015JD024658, URL http://dx.doi.org/10.1002/2015JD024658, 2015JD024658.

Sobel, A., S. Wang, and D. Kim, 2014: Moist static energy budget of the MJO during DYNAMO. *J. Atmos. Sci.*, **71 (11)**, 4276–4291.

Stano, G., T. N. Krishnamurti, T. S. V. V. Kumar, and A. Chakraborty, 2002: Hydrometeor structure of a composite monsoon depression using the trmm radar. *Tellus A*, **54 (4)**, 370–381, doi:10.1034/j.1600-0870.2002.01330.x, URL http://dx.doi.org/10.1034/j.1600-0870.2002.01330.x.

Warner, C., 1984: Core structure of a bay of bengal monsoon depression. *Monthly Weather Review*, **112 (1)**, 137–152, doi:10.1175/1520-0493(1984)112⟨0137:CSOABO⟩2.0.CO;2, URL https://doi.org/10.1175/1520-0493(1984)112⟨0137:CSOABO⟩2.0.CO;2, https://doi.org/10.1175/1520-0493(1984)112⟨0137:CSOABO⟩2.0.CO;2.

Wheeler, M., and G. N. Kiladis, 1999: Convectively coupled equatorial waves: Analysis of clouds and temperature in the wavenumber-frequency domain. *J. Atmos. Sci.*, **56**, 374–399, doi:10.1175/1520-0469(1999)056⟨0374:CCEWAO⟩2.0.CO;2.

Wing, A. A., and K. A. Emanuel, 2014: Physical mechanisms controlling self-aggregation of convection in idealized numerical modeling simulations. *J. Adv. Model. Earth Syst.*, **6 (1)**, 59–74.

Wolding, B. O., E. D. Maloney, and M. Branson, 2016: Vertically resolved weak temperature gradient analysis of the madden-julian oscillation in sp-cesm. *Journal of Advances in Modeling Earth Systems*, n/a–n/a, doi:10.1002/2016MS000724, URL http://dx.doi.org/10.1002/2016MS000724.

Yoon, J.-H., and T.-C. Chen, 2005: Water vapor budget of the indian monsoon depression. *Tellus A*, **57 (5)**, 770–782, doi:10.1111/j.1600-0870.2005.00145.x, URL http://dx.doi.org/10.1111/j.1600-0870.2005.00145.x.

Yoon, J.-H., and W.-R. Huang, 2012: *02 Indian Monsoon Depression: Climatology and Variability*. InTech.

Zhao, M., and Coauthors, 2017a: The GFDL Global Atmosphere and Land Model AM4.0/LM4.0: Documentation and Simulations with Prescribed SSTs Part I: Simulation Characteristics. *J. Adv. Model. Earth Syst.*

Zhao, M., and Coauthors, 2017b: The GFDL Global Atmosphere and Land Model AM4.0/LM4.0: Documentation and Simulations with Prescribed SSTs Part II: Model Description, Sensitivity Studies, and Tuning. *J. Adv. Model. Earth Syst.*

List of Figures

11 As in Fig. 9 but the shaded fields show (a) horizontal advection of low-frequency MSE by the high-frequency winds, (b) horizontal advection of high-frequency MSE by the low-frequency winds, (c) horizontal advection of high-frequency MSE advection by the high-frequency winds and (d) the sum of (a)-(c). The 850 hPa anomalous horizontal winds is shown as arrows. 40

12 (a) As in Fig. 5c but showing column-averaged $-\omega$ as a solid line, $-\omega'_a$ in red, $\omega'_c + \omega'_r$ in blue, and the residual $\omega' - \omega'_a - \omega'_c - \omega'_r$ as a dotted line. (b) Column-integrated vertical moisture advection by ω'_a (red solid) and $\partial\langle q'\rangle/\partial t$ (dotted line). 41

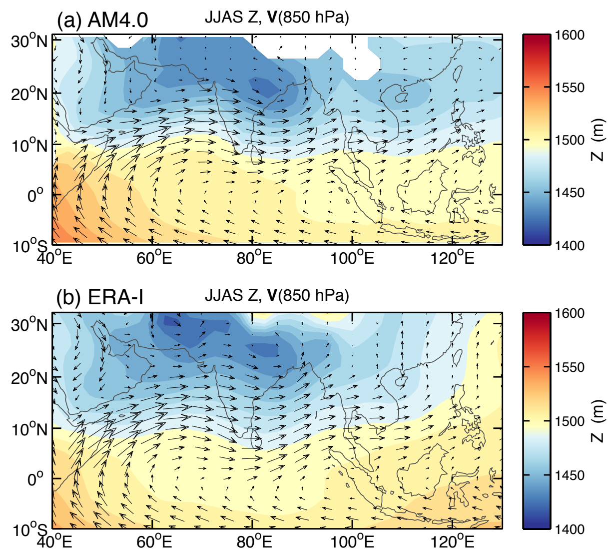

FIG. 1. Mean JJAS geopotential height (shading) and horizontal flow (arrows) for AM4.0 (top) and ERA-Interim (bottom). The longest arrows correspond to winds of $\sim$15 m s^{-1}. Blank shading in the top panel corresponds to regions where the Z field is beneath the surface.

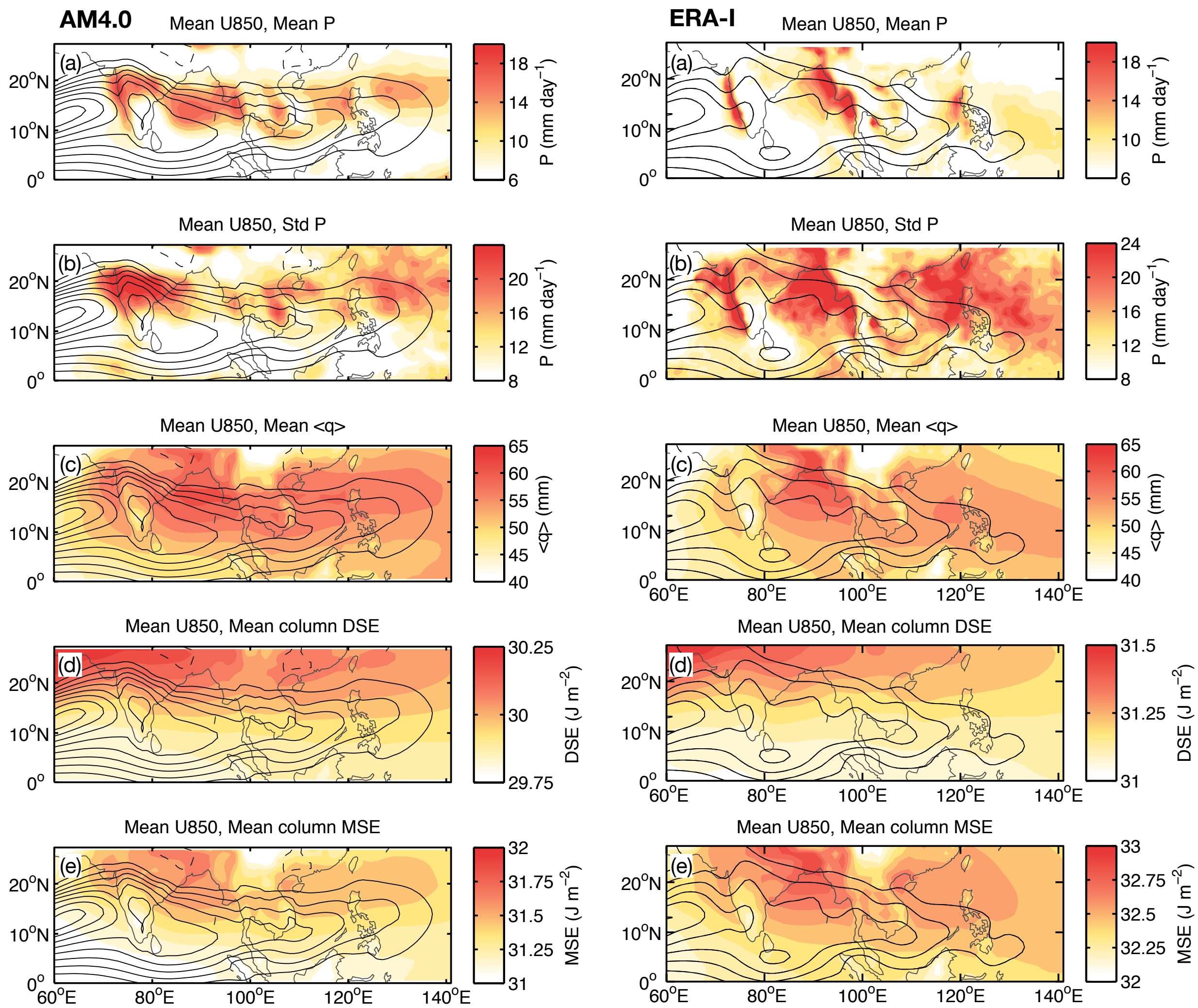

FIG. 2. Mean JJAS zonal wind (contours) and (a) mean JJAS precipitation, (b) standard deviation of JJAS precipitation, (c) JJAS column-integrated water vapor $\langle q \rangle$, (d) column DSE and (e) column MSE for (left) AM4.0 and (right) ERA-Interim/TRMM. Contour interval 2.5 m s^{-1}. Panels (d) and (e) are scaled by a factor of 10^8.

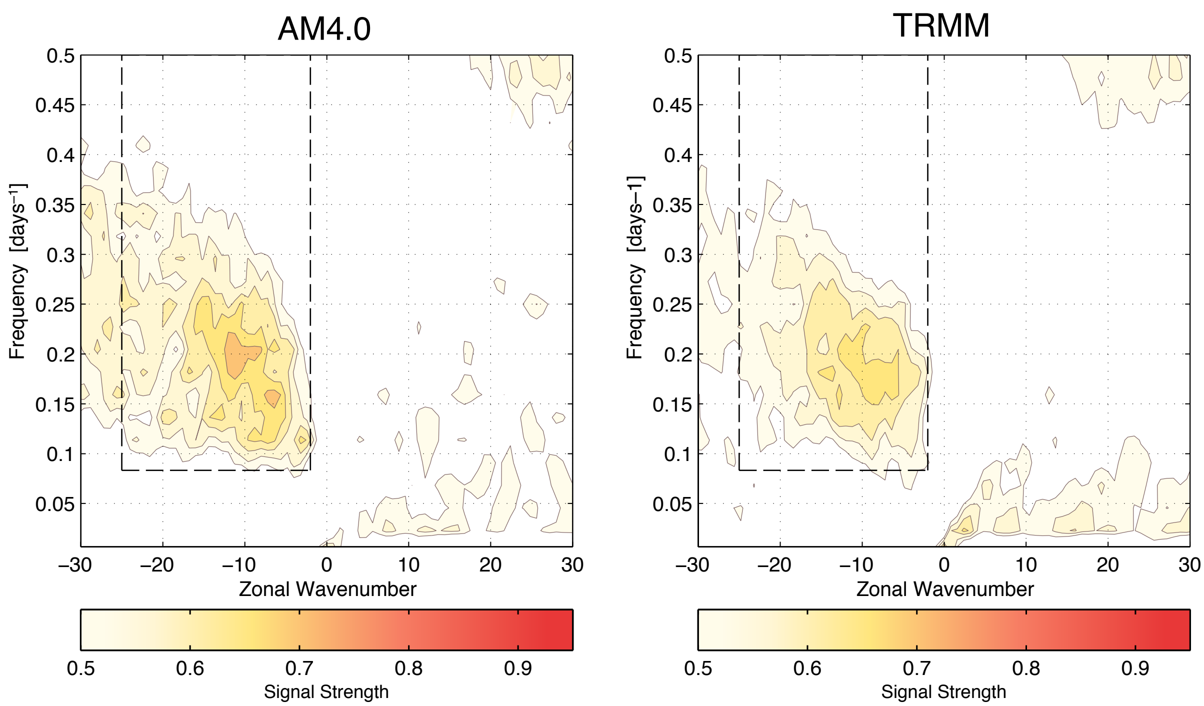

FIG. 3. Signal strength of (a) AM4.0 and (b) TRMM-3B42 precipitation. The signal was obtained from data around the 10-25°N latitude belt, and longitudinally tapered to emphasize the Asian monsoon region over 50-150°E. The dashed lines highlight the box used to define the filter used to analyze SMDs in this study.

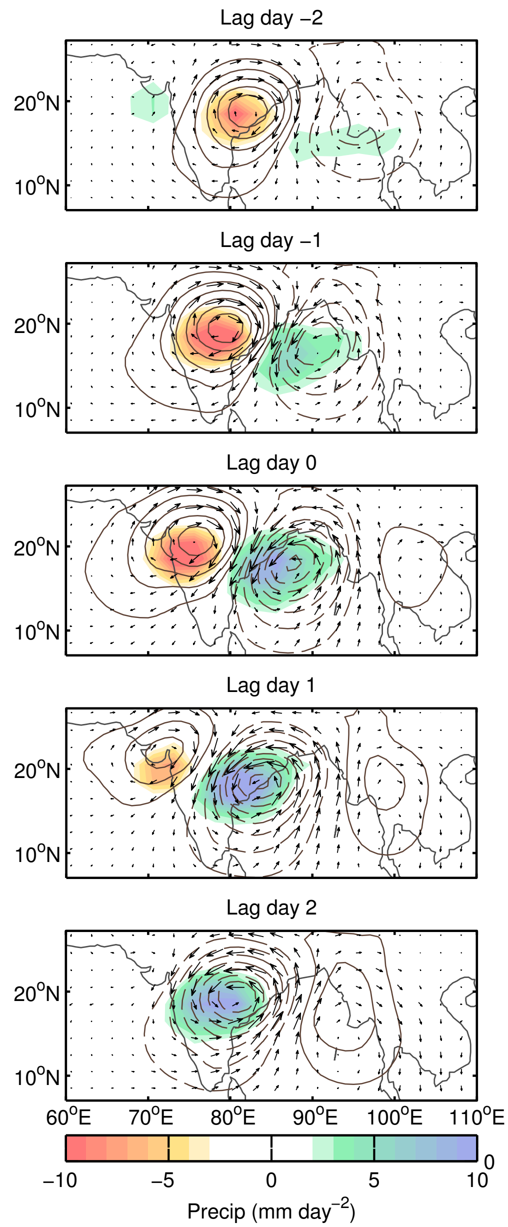

FIG. 4. Five panel sequence of AM4.0 anomalous precipitation (shading), 850 hPa Z' (contoured) and the anomalous horizontal winds (arrows) regressed onto precipitation data filtered to retain timescales shorter than 15 days and westward-propagating zonal wavenumbers 3-25, averaged over 15-20°N and 85-90°E. Each panel corresponds to lag regression at days -2,-1,0,1,2. The contour interval is 1.5 m.

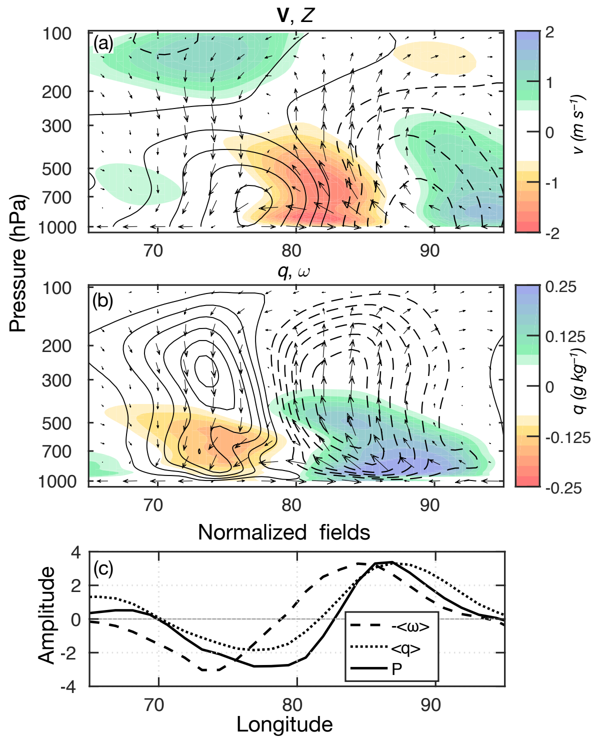

Fig. 5. Longitude-height cross section of a monsoon low-pressure system averaged over the 10-25°N latitude belt. (a) Meridional wind (shading) and geopotential height (contoured) anomalies. Contour interval is 1.5 m. (b) Specific humidity q (shading) and vertical velocity (contours). Contour interval is 5 hPa day^{-1}. The largest zonal flux vector is about 0.5 kg m^{-2} s^{-1}, and the largest vertical flux vector is about 0.001 kg m^{-2} s^{-1}. Panel (c) shows anomalous column-averaged vertical velocity, precipitation and column water vapor averaged over the 10-25°N latitude belt. The fields have been normalized by their standard deviation to facilitate comparison.

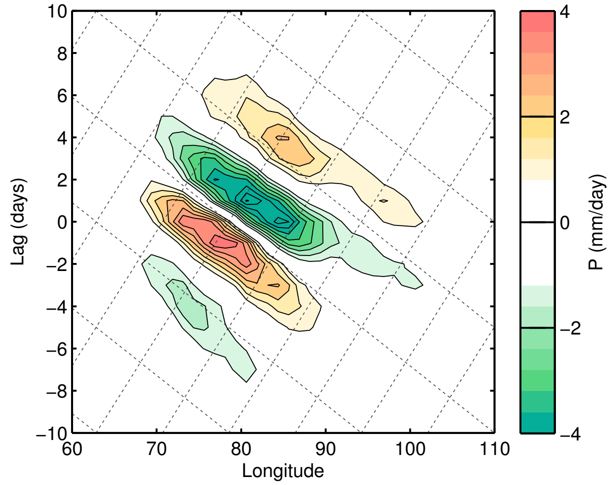

FIG. 6. Time-longitude diagram of anomalous precipitation obtained from a lag regression of the SMD index described in Section 2. The fields have been averaged over the 10-25°N latitude belt. Contour interval 0.2 mm day^{-1}. The dotted lines are lines of constant speeds of -4 m s^{-1} and 2 m s^{-1}.

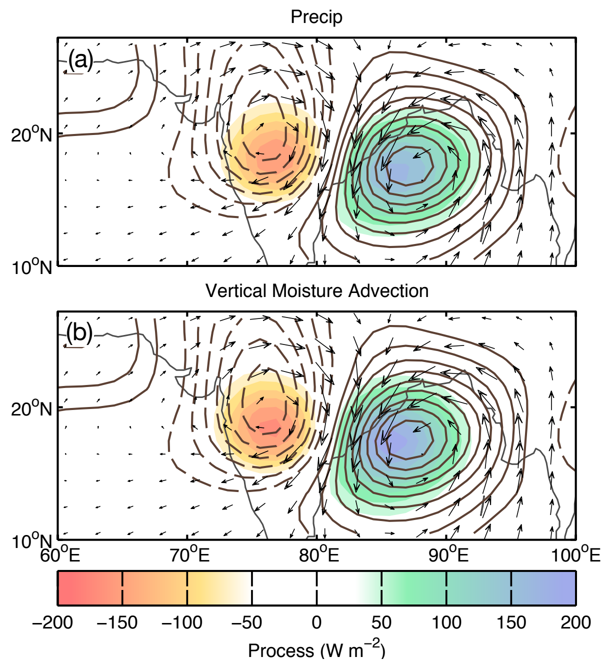

FIG. 7. SMD composite of anomalous column-integrated water vapor (contours) and anomalous precipitation (shading in a) and column-integrated vertical moisture advection (shading in b). Contour interval 0.25×10^6 J m^{-2}. The SMD composite is constructed by generating multiple regression maps from SMD indices that are slightly shifted in space (see Section 2b). Each of these maps is then shifted such that the center of the moisture/MSE anomalies is centered over the 85-90°E, 15-20°N box. The SMD composite is an average of all the regression maps. The terms are multiplied by $L_v = 2.5 \times 10^6$ J kg^{-1} to facilitate comparison with the MSE budget. The 850 hPa anomalous horizontal winds is shown as arrows in both panels.

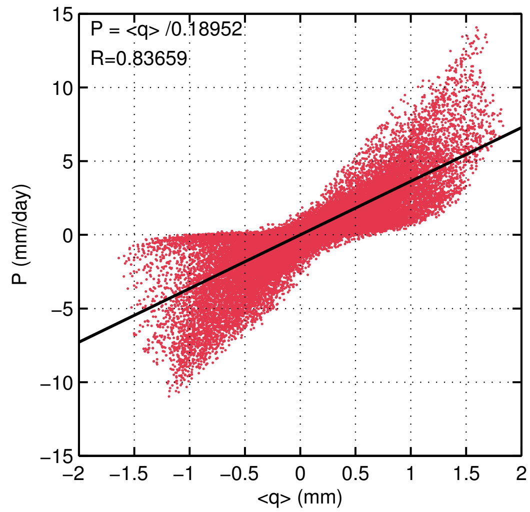

FIG. 8. Scatterplot of anomalous column integrated water vapor $\langle q' \rangle$ and precipitation P' from all points within 10-25°N, 60-100°E domain in the regression maps that make up the SMD composite. The linear least squares fit line is shown in thick black. The slope of the linear fit is shown, in units of days, in the top left along with the linear correlation coefficient.

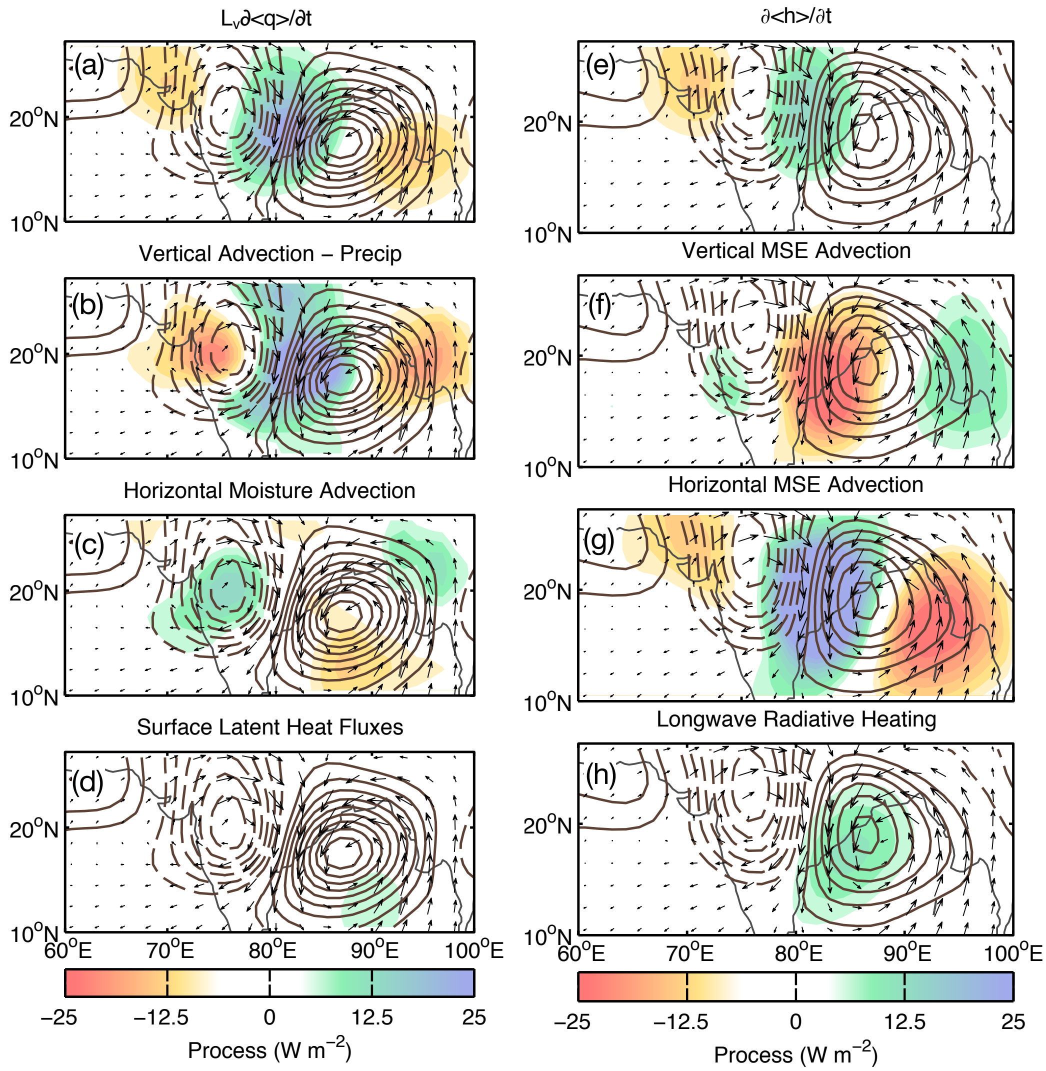

Fig. 9. SMD composite of the column-integrated moisture (left) and MSE (right) budgets. Panels (a)-(d) show column moisture as the contoured field and (a) the moisture tendency, (b) sum of vertical moisture advection and precipitation, (c) horizontal moisture advection and (d) surface latent heat fluxes as shaded fields. Panels (e)-(h) show column MSE as the contoured field (e) the column MSE tendency (f) Vertical MSE advection, (g) horizontal MSE advection, (h) longwave radiative heating as shading. Shading is in units of W m^{-2}. Contour interval 0.25 $\times$ 10^6 J m^{-2}. The 850 hPa anomalous horizontal winds is shown as arrows in all panels.

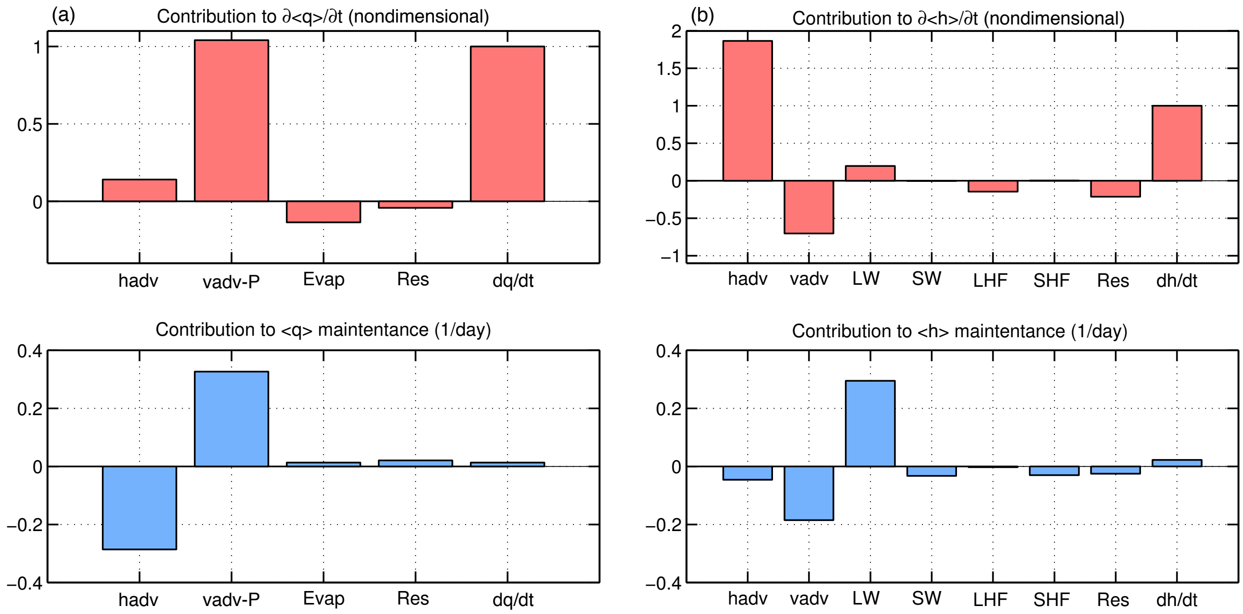

FIG. 10. Normalized contribution of the individual terms in the column-integrated moisture (a) and MSE budgets (b) to the maintenance (top) and propagation (bottom) of the regressed SMDs. The terms are obtained by projecting $\langle q' \rangle$ and $\langle h' \rangle$ (top panel) and $\partial \langle q' \rangle / \partial t$ and $\partial \langle h' \rangle / \partial t$ (bottom) onto the individual contributions to the moisture/MSE budget using Eq. (2). The terms of the moisture budget are (from left to right) horizontal moisture advection, the sum of vertical moisture advection and precipitation, surface evaporation, the residual after adding all terms, and the moisture tendency. The MSE budget terms are (from left to right) horizontal MSE advection, vertical MSE advection, longwave radiative heating, shortwave radiative heating, surface latent heat fluxes, surface sensible heat fluxes, the residual and the MSE tendency.

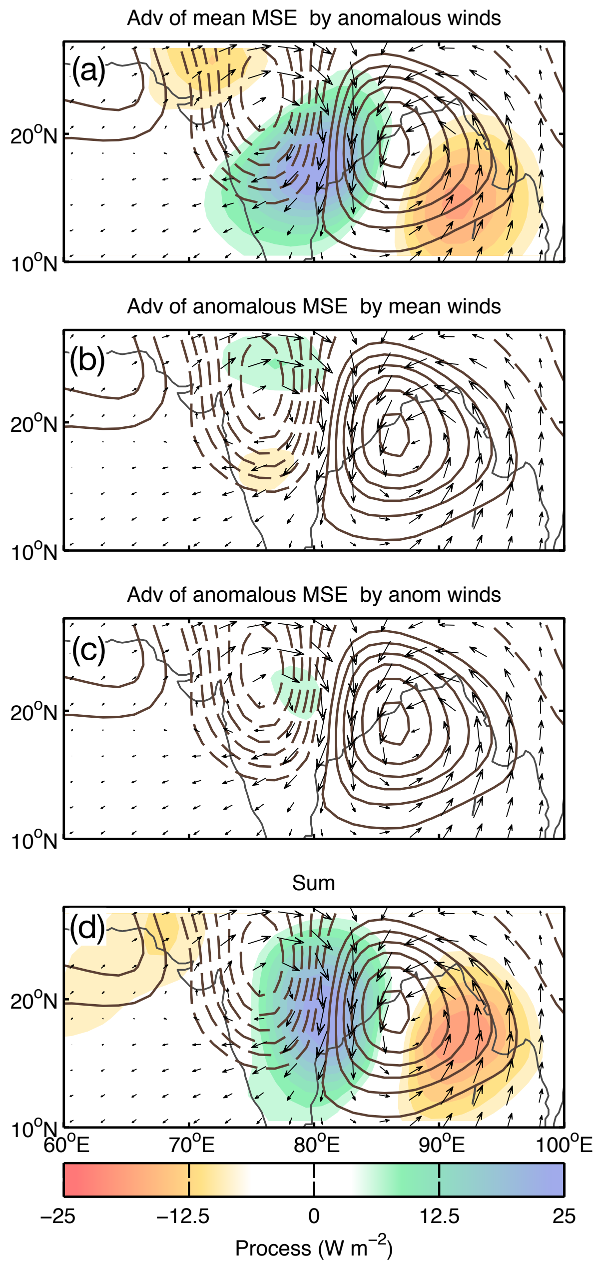

Fig. 11. As in Fig. 9 but the shaded fields show (a) horizontal advection of low-frequency MSE by the high-frequency winds, (b) horizontal advection of high-frequency MSE by the low-frequency winds, (c) horizontal advection of high-frequency MSE advection by the high-frequency winds and (d) the sum of (a)-(c). The 850 hPa anomalous horizontal winds is shown as arrows.

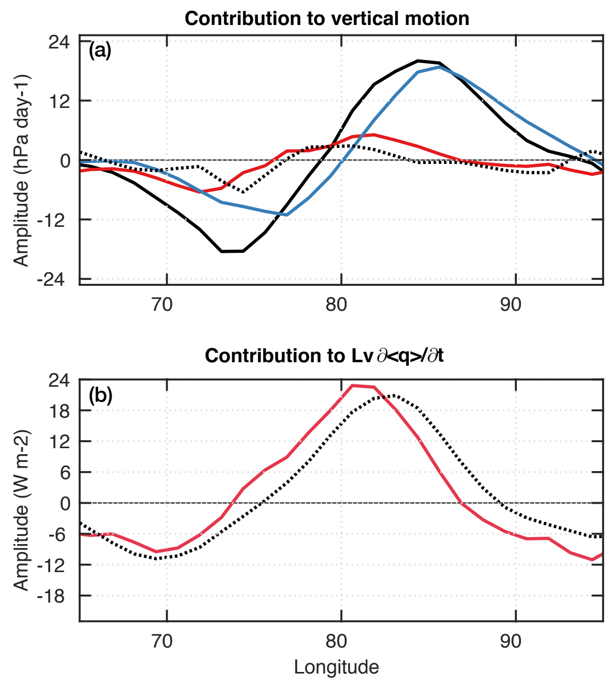

FIG. 12. (a) As in Fig. 5c but showing column-averaged $-\omega$ as a solid line, $-\omega_a'$ in red, $\omega_c' + \omega_r'$ in blue, and the residual $\omega' - \omega_a' - \omega_c' - \omega_r'$ as a dotted line. (b) Column-integrated vertical moisture advection by ω_a' (red solid) and $\partial\langle q'\rangle/\partial t$ (dotted line).